

## Research Article

# Wafer-Scale Synthesis of WS<sub>2</sub> Films with In Situ Controllable p-Type Doping by Atomic Layer Deposition

Hanjie Yang<sup>1</sup>, Yang Wang<sup>1</sup>, Xingli Zou<sup>2</sup>, Rongxu Bai<sup>1</sup>, Zecheng Wu<sup>1</sup>, Sheng Han<sup>1</sup>, Tao Chen<sup>1</sup>, Shen Hu<sup>1</sup>, Hao Zhu<sup>1</sup>, Lin Chen<sup>1</sup>, David W. Zhang<sup>1</sup>, Jack C. Lee<sup>3</sup>, Xionggang Lu<sup>2</sup>, Peng Zhou<sup>1</sup>, Qingqing Sun<sup>1</sup>, Edward T. Yu<sup>3</sup>, Deji Akinwande<sup>3</sup>, and Li Ji<sup>1</sup>

<sup>1</sup>State Key Laboratory of ASIC and System, School of Microelectronics, Fudan University, Shanghai 200433, China

<sup>2</sup>State Key Laboratory of Advanced Special Steel, School of Materials Science and Engineering, Shanghai University, Shanghai 200444, China

<sup>3</sup>Microelectronics Research Center, Department of Electrical and Computer Engineering, The University of Texas at Austin, Austin, 78758 Texas, USA

Correspondence should be addressed to Qingqing Sun; [qqsun@fudan.edu.cn](mailto:qqsun@fudan.edu.cn), Edward T. Yu; [ety@ece.utexas.edu](mailto:ety@ece.utexas.edu), Deji Akinwande; [deji@ece.utexas.edu](mailto:deji@ece.utexas.edu), and Li Ji; [nmgjili@gmail.com](mailto:nmgjili@gmail.com)

Received 30 August 2021; Accepted 9 November 2021; Published 6 December 2021

Copyright © 2021 Hanjie Yang et al. Exclusive Licensee Science and Technology Review Publishing House. Distributed under a Creative Commons Attribution License (CC BY 4.0).

Wafer-scale synthesis of p-type TMD films is critical for its commercialization in next-generation electro/optoelectronics. In this work, wafer-scale intrinsic n-type WS<sub>2</sub> films and in situ Nb-doped p-type WS<sub>2</sub> films were synthesized through atomic layer deposition (ALD) on 8-inch  $\alpha$ -Al<sub>2</sub>O<sub>3</sub>/Si wafers, 2-inch sapphire, and 1 cm<sup>2</sup> GaN substrate pieces. The Nb doping concentration was precisely controlled by altering cycle number of Nb precursor and activated by postannealing. WS<sub>2</sub> n-FETs and Nb-doped p-FETs with different Nb concentrations have been fabricated using CMOS-compatible processes. X-ray photoelectron spectroscopy, Raman spectroscopy, and Hall measurements confirmed the effective substitutional doping with Nb. The on/off ratio and electron mobility of WS<sub>2</sub> n-FET are as high as 10<sup>5</sup> and 6.85 cm<sup>2</sup> V<sup>-1</sup> s<sup>-1</sup>, respectively. In WS<sub>2</sub> p-FET with 15-cycle Nb doping, the on/off ratio and hole mobility are 10 and 0.016 cm<sup>2</sup> V<sup>-1</sup> s<sup>-1</sup>, respectively. The p-n structure based on n- and p-type WS<sub>2</sub> films was proved with a 10<sup>4</sup> rectifying ratio. The realization of controllable *in situ* Nb-doped WS<sub>2</sub> films paved a way for fabricating wafer-scale complementary WS<sub>2</sub> FETs.

## 1. Introduction

As silicon-based CMOS technology is reaching its physical limits, two-dimensional transition metal dichalcogenides (TMDs) have been intensively investigated as potential ultrathin channel materials for future electronics. TMDs show tunable bandgap, good air-stability, and high carrier mobility and can be applied in transistors [1–4], photodetectors [5], computing technologies [6, 7], memory [8, 9], RF [10–12], and heterojunction synapse [13, 14]. However, there are still many challenges, including (1) realization of large wafer-scale deposition, (2) a controllable p-type doping method for TMD films, (3) reducing Schottky barrier-induced Fermi level pinning at the metal/TMDs contacts, and (4) high-quality high-k/TMD interface. Chemical vapor deposition (CVD) is an effective way to synthesize single-

crystalline TMDs films [15–17], but wafer-scale deposition and precisely-controlled thickness of TMDs films are difficult to achieve via CVD. Because TMD films are too thin for p-type doping by ion implantation [18–21], a variety of different approaches have been pursued, including charge transfer doping by physical adsorption of molecules or salts on surface [22–25], and metal oxides (MoO<sub>3</sub>) [26] or metal-induced inversion (Tungsten) [27, 28] of WS<sub>2</sub> through interfacial interactions. However, it has proven difficult to precisely control the doping behaviors and consequently electronic device performance.

Atomic layer deposition (ALD), a self-limiting process with precisely controlled layer thickness, is an ideal technique to synthesize wafer-scale TMD films [29–32]. Niobium (Nb) has been demonstrated as an effective p-type dopant for WS<sub>2</sub> [33–35]. Halide-assisted CVD and low-pressure CVD have

been utilized to insert Nb atoms into the  $\text{WS}_2$  lattice [20, 36], and pulsed laser deposition (PLD) can also achieve p-type  $\text{WS}_2$  films using premelted Nb-doped targets, but without device demonstration [18]. However, neither CVD nor PLD is capable of *in situ* and controllable doping. ALD has been demonstrated for the synthesis of wafer-scale  $\text{WS}_2$  films with  $\text{WF}_6$  as a W precursor and  $\text{H}_2\text{S}$  as a S precursor [37, 38]. However, very few works have reported *in situ* controllable p-type-doped  $\text{WS}_2$  FETs through ALD [39].  $\text{NbS}_2$  can be synthesized by utilizing  $\text{NbCl}_5$  and HMDST in ALD, similar to  $\text{WS}_2$ . In addition, the lattice constants of  $2\text{H-NbS}_2$  ( $(a, b, c) = (0.332, 0.332, 1.194)$  nm) are close to those of  $2\text{H-WS}_2$  ( $(a, b, c) = (0.316, 0.316, 1.247)$  nm), which facilitates substitutional doping of Nb atoms into the  $\text{WS}_2$  lattice [40].

Here, in this work, we demonstrate for the first time the wafer-scale synthesis of  $\text{WS}_2$  films by ALD with controllable *in situ* p-type doping, on 8-inch  $\alpha\text{-Al}_2\text{O}_3/\text{Si}$  wafer, 2-inch sapphire wafers, and  $1\text{ cm}^2$  GaN substrate pieces. The growth mechanisms of ALD  $\text{WS}_2$  and *in situ* Nb doping were analyzed, and the doping concentration is shown to be controllable by altering Nb cycle numbers. Plan-view and cross-sectional TEM imaging reveals the layered structure of  $\text{WS}_2$ , and Hall effect measurements and TOF-SIMS confirm the effective incorporation of Nb dopants. Moreover, both  $\text{WS}_2$  n-FETs and Nb-doped  $\text{WS}_2$  p-FETs were fabricated by CMOS-compatible processes from as-prepared ALD-grown n- $\text{WS}_2$  and Nb-doped p- $\text{WS}_2$  films. The on/off ratio and electron mobility of  $\text{WS}_2$  n-FET were up to  $10^5$  and  $6.85\text{ cm}^2\text{ V}^{-1}\text{ s}^{-1}$ , while the on/off ratio and hole mobility of Nb-doped  $\text{WS}_2$  p-FET were  $10^1$  and  $0.016\text{ cm}^2\text{ V}^{-1}\text{ s}^{-1}$ , respectively.  $\text{WS}_2$  FETs with different concentrations of Nb dopants were also investigated. Our work, by demonstrating *in situ* controllable Nb-doped  $\text{WS}_2$  films and consequently p-FETs, helps establish a path to fabricate complementary  $\text{WS}_2$  FETs at wafer-scale volumes.

## 2. Results

**2.1. Growth Mechanisms.** Figure 1(a) illustrates the mechanisms of the ALD process for  $\text{WS}_2$  growth and *in situ* Nb doping. The reactor temperature was  $400^\circ\text{C}$ , while the  $\text{WCl}_6$  (99.9%),  $\text{NbCl}_5$ , and HMDST (98%) were kept at  $93^\circ\text{C}$ ,  $60^\circ\text{C}$ , and room temperature, respectively. One cycle of  $\text{WS}_2$  deposition includes 1 s  $\text{WCl}_6$  pulse, followed by 8 s purge (Argon, 99.99%), and 1 s HMDST pulse, followed by 5 s purge, sequentially. For Nb doping,  $\text{NbCl}_5$  and HMDST are used as precursors. One cycle of  $\text{NbS}_2$  deposition includes 1 s  $\text{NbCl}_5$  pulse, followed by 8 s purge (Argon, 99.99%), and 1 s HMDST pulse, followed by 5 s purge. The growth rate of  $\text{WS}_2$  film was calibrated to about  $0.036\text{ nm/cycle}$ . To realize a controllable *in situ* doping,  $\text{WCl}_6$  pulses were replaced by  $\text{NbCl}_5$  pulses, and the doping concentration could thus be adjusted by varying  $\text{NbCl}_5$  pulse numbers. Figure 1(b) shows photographs of wafer-scale 400-cycle  $\text{WS}_2$  films deposited on 8-inch amorphous- $\text{Al}_2\text{O}_3/\text{Si}$  wafer, 2-inch sapphire wafer, and pieced GaN substrate with good uniformity. Raman spectra of 400-cycle annealed  $\text{WS}_2$  films at  $950^\circ\text{C}$  are shown in Figure 1(c), confirming that high-

quality  $\text{WS}_2$  could be deposited on all these substrates except for Si with different thickness at 400 cycles. In view of this, we use sapphire as the substrate for this research.

**2.1.1. ALD-Deposited  $\text{WS}_2$  Film.** At the initial stage, the  $\text{WCl}_6$  and HMDST vapor were exposed directly onto the sapphire substrates and  $\text{WS}_2$  layers were formed laterally on sapphire substrates. The subsequent layers were deposited onto the initial  $\text{WS}_2$  layer to connect the isolated flakes and form films. Considering this, a postannealing process would be beneficial for improving film quality. The as-deposited  $\text{WS}_2$  films were annealed at  $950^\circ\text{C}$  for 2 h in sulfur atmosphere. The XPS spectra of as-deposited and annealed  $\text{WS}_2$  films are shown in Figure 2(a). The fine spectra of as-deposited  $\text{WS}_2$  contained two pairs of W 4f peaks, representing  $\text{WS}_3$  and  $\text{WS}_2$ , respectively. The higher coordination number of W atom in  $\text{WS}_3$  than that in  $\text{WS}_2$  results a shift towards higher binding energy, with the binding energies of  $\text{W}^{6+}\text{f}_{5/2}$  and  $\text{W}^{6+}\text{f}_{7/2}$  being 38.7 eV and 36.68 eV and those of  $\text{W}^{4+}\text{f}_{5/2}$  and  $\text{W}^{4+}\text{f}_{7/2}$  being 35.22 eV and 33.08 eV, respectively. Similarly, the fine spectra of as-deposited  $\text{WS}_2$  showed two pairs of S 2p peaks. The positions of the  $\text{S}_2\text{ 2p}^{1/2}$  and  $\text{S}_2\text{ 2p}^{3/2}$  peaks for  $\text{W}^{6+}$ -S bonding were at 164.54 eV and 163.54 eV, while the positions of the  $\text{S}_1\text{ 2p}^{1/2}$  and  $\text{S}_1\text{ 2p}^{3/2}$  peaks for  $\text{W}^{4+}$ -S bonding were at 164.02 eV and 163.04 eV, respectively. XPS analysis for as-deposited  $\text{WS}_2$  films shows the films to be a mixture of  $\text{WS}_2$  and  $\text{WS}_3$ , and the stoichiometric ratio of W/S was about 1:2.7. A postannealing process in S atmosphere at  $950^\circ\text{C}$  for 2 hours improves film crystallinity. After annealing, the fine spectra of W 4f exhibited only one pair of  $\text{W 4f}_{5/2}$  and  $\text{W 4f}_{7/2}$  peaks, indicating  $\text{WS}_3$  components decomposed to  $\text{WS}_2$ , along with a similar result for S 2p spectra, both without characteristic peaks indicative of  $\text{W}^{6+}$ -S bonding. As a result, the stoichiometric ratio of W/S was reduced to 1:2.1, with the help of desulfurization and improved film crystallinity. The full spectra of as-deposited and annealed  $\text{WS}_2$  are shown in Fig. S2. To further investigate the crystallinity of as-deposited and annealed  $\text{WS}_2$  films, Raman spectroscopy was performed. After annealing, the relative intensity of the  $\text{A}_{1g}$  and  $\text{E}_{2g}^1+2\text{LA(M)}$  peaks for annealed  $\text{WS}_2$  was much higher than that of as-deposited  $\text{WS}_2$  (Fig. S3), confirming the improved film crystallinity after annealing. Therefore, subsequent  $\text{WS}_2$  films in this paper have undergone a postannealing process. In addition, when increasing  $\text{WS}_2$  film thickness from 250 cycle to 500 cycle, the separation between the  $\text{A}_{1g}$  and  $\text{E}_{2g}^1+2\text{LA(M)}$  peaks increased from  $64.2\text{ cm}^{-1}$  to  $69.5\text{ cm}^{-1}$ , demonstrating good thickness controllability for ALD grown  $\text{WS}_2$ , as shown in Figure 2(b). Plan-view and cross-sectional TEM imaging shown in Figure 2(c) reveal a continuous planar film, without warpages or kink formation. The thickness of the annealed 400-cycle  $\text{WS}_2$  film was 4.6 nm, and a cross-sectional TEM image of a 3.7 nm  $\text{WS}_2$  film is shown in Fig. S4. Preparing monolayer films is very challenging due to the growth mechanism of ALD TMD films. From the plane-view TEM and SAED patterns results, out of 259  $\text{WS}_2$  analyzed grains, the average grain size was 55 nm (details of grain size were shown

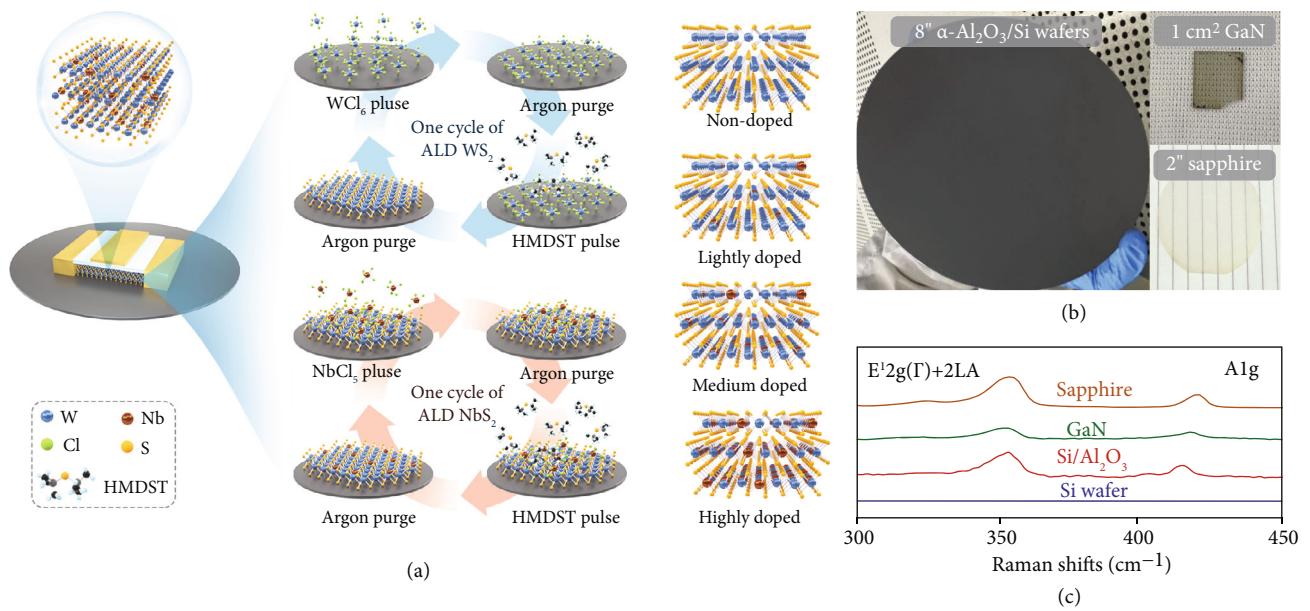


FIGURE 1: Illustration of ALD growth mechanisms and characterizations. (a) Idealized schematic of the mechanisms of ALD process for WS<sub>2</sub> growth and in situ Nb doping. The doping concentration could be controlled by adjusting NbS<sub>2</sub> cycle numbers. (b) Photographs of 400-cycle WS<sub>2</sub> films deposited on 8-inch  $\alpha$ -Al<sub>2</sub>O<sub>3</sub>/Si wafer, 2-inch sapphire wafer, and pieced GaN substrates. (c) The Raman spectra of annealed WS<sub>2</sub> on Si/Al<sub>2</sub>O<sub>3</sub>, GaN, and sapphire confirm the successful synthesis of WS<sub>2</sub> on each substrate surface.

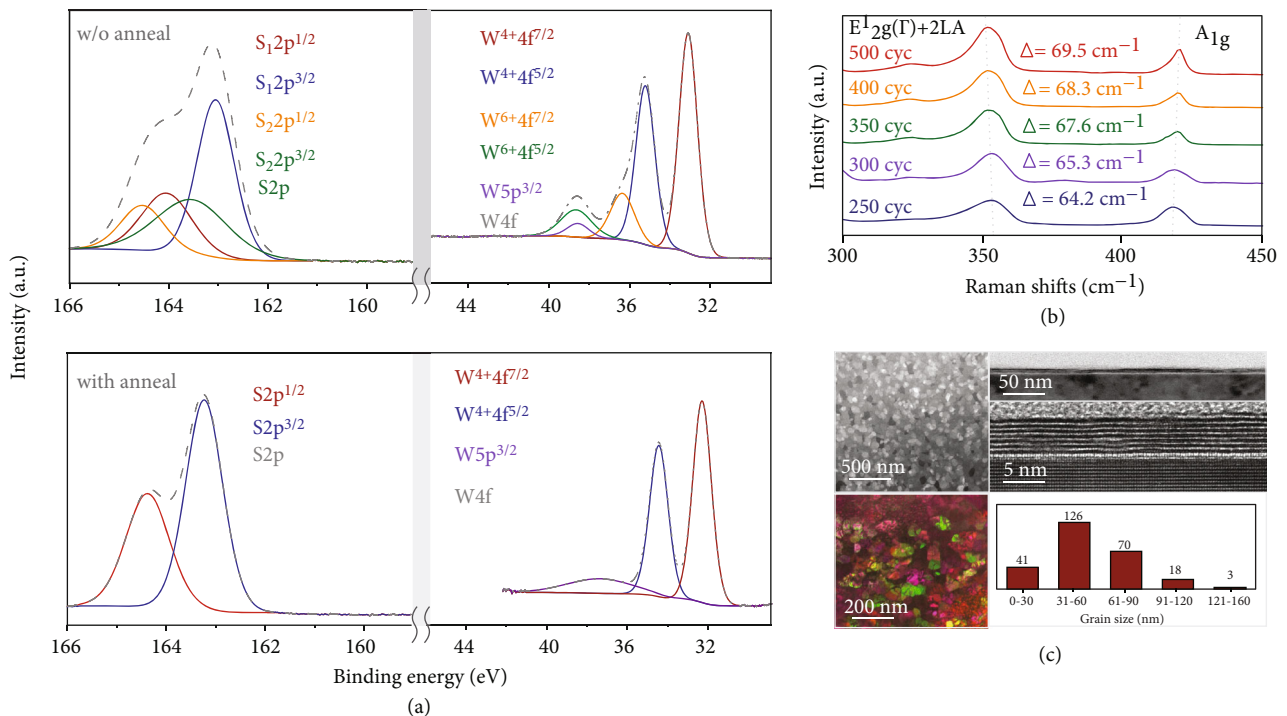


FIGURE 2: Material characterizations of ALD grown WS<sub>2</sub> films without doping. (a) The XPS fine spectra of W 4f and S 2p for as-deposited and annealed 400-cycle WS<sub>2</sub> film. Both WS<sub>2</sub> and WS<sub>2+x</sub> peaks were observed, with the W/S ratio of 1:2.7. Only WS<sub>2</sub> was observed in fine spectra of annealed WS<sub>2</sub>, indicating the necessity of annealing, and the W/S ratio was reduced to 1:2.1. (b) The Raman spectra of annealed WS<sub>2</sub> films with varying thickness. The Raman peak separation increased with increasing film thickness. (c) The plane-view and cross-sectional TEM result of 400-cycle annealed WS<sub>2</sub> film and the plane-view TEM result and statistical analysis of film grains by selected area electron diffraction (SAED) patterns. A layered structure was clearly observed in cross-sectional TEM. The average grain size of 259 WS<sub>2</sub> grains was 55 nm, with the maximum size up to 160 nm.



in Fig. S5), while the largest grain size was as high as 160 nm. The AFM image of 4.6 nm  $\text{WS}_2$  film is shown in Fig. S6.

**2.1.2. In Situ Niobium-Doped p-Type  $\text{WS}_2$  Films.** Pure  $\text{NbS}_2$  films were deposited by ALD using  $\text{NbCl}_5$  and HMDST precursors, and the XPS results of as-deposited  $\text{NbS}_2$  films are shown in Fig. S7. The Nb doping process is illustrated in Fig. S8 and Table S1. as-deposited and annealed 400-cycle  $\text{WS}_2$  films with 30-cycle Nb doping were then investigated by XPS. In the fine spectra of W 4f peaks (Figure 3(a)) of as-deposited Nb-doped  $\text{WS}_2$  films, two pairs of characteristic peaks revealing both  $\text{W}^{6+}$ -S bonding and  $\text{W}^{4+}$ -S bonding were observed. However, different from the fine spectra of S 2p of as-deposited  $\text{WS}_2$ , a pair of characteristic peaks of Nb-S bonding was also observed, indicating successful Nb substitutional incorporation. The fine spectra of Nb 3d confirmed the presence of  $\text{NbS}_2$  as well. After annealing, only  $\text{W}^{4+}$ -S bonding was observed in the W 4f fine spectra (see Figure 3(a)), while  $\text{W}^{4+}$ -S bonding and Nb-S bonding were both observed in the S 2p fine spectra. The Nb 3d fine spectra proved the formation of  $\text{NbS}_2$ , indicating that Nb atoms were substituted into  $\text{WS}_2$  lattice. The stoichiometric ratio of Nb/S was about 1:2.0, while that of W/S was 1:2.1. The full spectra of as-deposited and annealed Nb-doped  $\text{WS}_2$  are shown in Fig. S9. The Raman spectra of annealed Nb-doped 400-cycle  $\text{WS}_2$  films with Nb doping varying from 10 cycles to 100 cycles are shown in Figure 3(b). From the spectra, the blue shift of the  $\text{A}_{1g}$  peaks was obvious, especially in the Nb-doped  $\text{WS}_2$  film with 100-cycle Nb doping, which implies stiffening of the Nb-doped  $\text{WS}_2$  lattice with Nb-S bonds [18]. The annealing process was necessary for Nb atoms to be activated and incorporated substitutionally into the  $\text{WS}_2$  lattice. The plan-view EDX mapping results are shown in Fig. S10, confirming successful Nb doping of the  $\text{WS}_2$  film.

Hall effect measurements of undoped  $\text{WS}_2$  and Nb-doped  $\text{WS}_2$  with 30-cycle Nb doping were performed at temperatures ranging from 50 K to 300 K. As shown in Figure 3(c), the carrier type of undoped  $\text{WS}_2$  was electrons, while the carrier type of Nb-doped  $\text{WS}_2$  film was holes, confirming the effective Nb-substitutional doping. The hall mobility of undoped  $\text{WS}_2$  was up to  $147.9 \text{ cm}^2 \text{ V}^{-1} \text{ s}^{-1}$  at 50 K and  $86.3 \text{ cm}^2 \text{ V}^{-1} \text{ s}^{-1}$  at 300 K, while the hall mobility of Nb-doped  $\text{WS}_2$  was  $12.4 \text{ cm}^2 \text{ V}^{-1} \text{ s}^{-1}$  at 50 K and  $3.6 \text{ cm}^2 \text{ V}^{-1} \text{ s}^{-1}$  at 300 K, respectively. The resistivity of Nb-doped  $\text{WS}_2$  was 4 orders of magnitude higher than that of  $\text{WS}_2$ , which revealed the fact that the Nb atom was effectively doped to substitute W atom in  $\text{WS}_2$  lattice.

As shown in Figure 3(d), the Hall mobility and resistivity of Nb-doped  $\text{WS}_2$  films with Nb doping of 15, 20, and 100 cycles at 300 K and TOF-SIMS of pristine  $\text{WS}_2$  and Nb-doped  $\text{WS}_2$  with Nb doping of 20 and 100 cycles were investigated as well. With increasing Nb concentration, the hall mobility decreased from  $12.60 \text{ cm}^2 \text{ V}^{-1} \text{ s}^{-1}$  to  $5.73 \text{ cm}^2 \text{ V}^{-1} \text{ s}^{-1}$ , while the resistivity of 15-cycle Nb-doped  $\text{WS}_2$  film was 3 orders of magnitude higher than that of 100-cycle Nb-doped  $\text{WS}_2$  film. This result implied that 100-cycle Nb-doped  $\text{WS}_2$  was heavily p-doped. Nb secondary

ion intensity of pristine  $\text{WS}_2$  film was normalized to 1, while the Nb intensity of Nb-doped  $\text{WS}_2$  films with Nb doping of 20 and 100 cycles was normalized as 5.13 and 19.25. The increased normalized Nb intensity implied the rising doping concentration with the increase of Nb cycle number. Both Hall effect results and TOF-SIMS gave evidence of *in situ* controllable and substitutional Nb doping. An accurate quantitative value of concentration of Nb doping could not be obtained due to the poor detection accuracy and low atom collection efficiency. STEM is not applicable for ALD grown Nb-doped  $\text{WS}_2$  films, due to the nature of polycrystalline films yielding only the statistical results within few layers. Raw data of Hall measurements of  $\text{WS}_2$  and Nb-doped  $\text{WS}_2$  with in Figure 3(d) are shown in Table S2.

**2.1.3. Electrical Properties of  $\text{WS}_2$  n-FET and Nb-Doped  $\text{WS}_2$  p-FET.** To characterize the electrical properties of 4.6 nm  $\text{WS}_2$  n-FETs and Nb-doped  $\text{WS}_2$  p-FETs, top-gate transistors were fabricated with  $2 \mu\text{m}$  gate width on sapphire substrate. The CMOS-compatible process flow and the structure of top-gate FET are shown in Figure 4(a) (detailed process was discussed in Materials and Methods). ALD  $\text{Al}_2\text{O}_3$  films (20 nm) were used as high-k dielectrics. The equivalent oxide thickness was 13 nm. The transfer characteristic of 8-layer  $\text{WS}_2$  n-FET is shown in Figure 4(b), with  $V_d$  varying from 0.1 V to 0.5 V, while the output characteristics with  $V_g$  vary from 1 V to 5 V. The transfer on-current of  $\text{WS}_2$  n-FET reached as high as  $0.4 \mu\text{A}/\mu\text{m}$  at  $V_d = 0.5 \text{ V}$ , and the on-off ratio was up to  $10^5$ . The detailed mobility of 30 tested  $\text{WS}_2$  n-FETs is also plotted in Figure 4(b). The maximum and minimum mobilities of n-FETs were  $6.85 \text{ cm}^2 \text{ V}^{-1} \text{ s}^{-1}$  and  $0.32 \text{ cm}^2 \text{ V}^{-1} \text{ s}^{-1}$ , respectively, while the median mobility was  $3.58 \text{ cm}^2 \text{ V}^{-1} \text{ s}^{-1}$ . The mobility of over 70% of  $\text{WS}_2$  n-FETs was in the range of 1 to  $5 \text{ cm}^2 \text{ V}^{-1} \text{ s}^{-1}$ .

The transfer characteristic of a 4.6 nm Nb-doped  $\text{WS}_2$  p-FET with 15-cycle Nb doping with  $V_d$  varying from 0.1 V to 0.5 V and the output characteristics with  $V_g$  varying from -2 V to -6 V are shown in Figure 4(c). Compared to the  $\text{WS}_2$  n-FET, the carrier type changed from electron to hole, which proved the Nb substituted for W atom in  $\text{WS}_2$  lattice. The on- and off-current of Nb-doped  $\text{WS}_2$  p-FET was only  $5 \times 10^{-2}$  at  $V_d = 0.5 \text{ V}$ , far less than that of  $\text{WS}_2$  n-FET. However, the hole mobility of Nb-doped  $\text{WS}_2$  p-FET was  $0.016 \text{ cm}^2 \text{ V}^{-1} \text{ s}^{-1}$ , while the on/off ratio was  $10^1$ . For Hall effect measurements, the resistivity of 15-cycle Nb-doped  $\text{WS}_2$  was 5 orders of magnitude higher than that of undoped  $\text{WS}_2$ , and the mobility of 15-cycle Nb-doped  $\text{WS}_2$  was far less than that of undoped  $\text{WS}_2$  at 300 K. The field-effect mobility of  $\text{WS}_2$  FETs was smaller than the Hall effect of  $\text{WS}_2$ , due to the influence of transistors' electrical contacts on the underestimation of field-effect mobility. The Hall mobility was roughly estimated through field-effect mobility due to the nonlinear dependence of carrier concentration on gate voltage [41]. Moreover, the stability of our process was inquired through measuring the on-current of Nb-doped  $\text{WS}_2$  p-FET with gate length varying from  $5 \mu\text{m}$  to  $50 \mu\text{m}$ . (Figure 4(c)). The distribution of  $I_{d,\text{sat}}$  (at  $V_g = -4 \text{ V}$ ,  $V_d = 0.5 \text{ V}$ ) amongst 132 Nb-doped  $\text{WS}_2$  p-FET with 20-cycle Nb doping on the

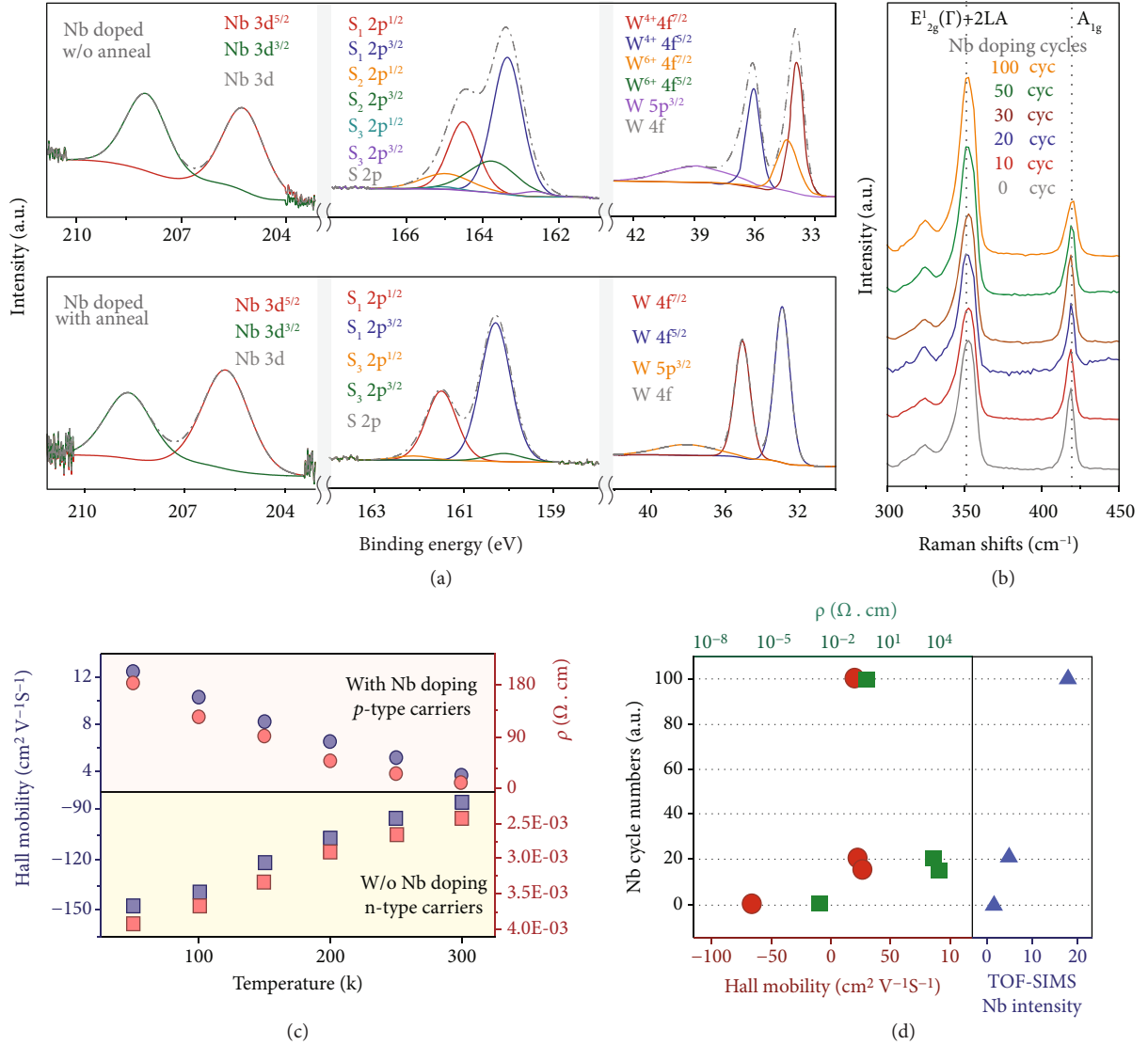


FIGURE 3: Material characterization of Nb-doped p-type WS<sub>2</sub>. (a) The XPS fine spectra of as-deposited and annealed 400-cycle WS<sub>2</sub> with 30-cycle Nb doping. WS<sub>2</sub>, WS<sub>2+x</sub>, and NbS<sub>2</sub> were all observed in as-deposited Nb-doped WS<sub>2</sub> film. After annealing, only WS<sub>2</sub> and NbS<sub>2</sub> were observed, indicating the effective doping. (b) The Raman spectra of 400-cycle WS<sub>2</sub> with Nb doping varying from 10 to 100 cycles. A blue shift of A<sub>1g</sub> peak was observed when increasing doping concentration, implying the stiffening of Nb-doped WS<sub>2</sub> lattice with Nb-S bonds. (c) The hall mobility and resistivity of WS<sub>2</sub> and Nb-doped WS<sub>2</sub> with 50-cycle Nb doping at temperature varying from 50 K to 300 K. (d) The mobility, resistivity, and TOF-SIMS of WS<sub>2</sub> and Nb-doped WS<sub>2</sub> with Nb doping of 15, 20, and 100 cycles. After 15-cycle Nb doping, the carrier type changed from electrons to holes, and the mobility decreased one order of magnitude, while the resistivity increased 4 orders of magnitude. However, with increasing Nb doping, the mobility continued to decrease, while the resistivity started to decrease. The normalized Nb secondary ion intensity of Nb-doped WS<sub>2</sub> films indicated the occurrence of p-type doping.

same day was summarized. With increasing gate length,  $I_{d,sat}$  decreased, suggesting the fabrication process was well-controlled and uniform. To explore the controllability of Nb doping, the transfer characteristics of Nb-doped WS<sub>2</sub> FETs with Nb doping varying from 1 cycle to 20 cycles were measured (Figure 4(d)). Nb-doped WS<sub>2</sub> FET did not show p-type behavior but with a decreased on- and off-current until reaching 15 cycles. When further increasing Nb concentrations, the current of p-FET increased and the on/off ratio decreased in that the resistivity and mobility of Nb-doped WS<sub>2</sub> film decreased, which was identical to the hall

effect measurements. The WS<sub>2</sub> FET was heavily p-doped after 20-cycle Nb doping. These results proved the good controllability of in situ Nb doping by ALD.

Due to the lack of dangling bonds at the surface of WS<sub>2</sub>, it was difficult to deposit very high quality high-k dielectrics. Thus, the PBTI of WS<sub>2</sub> n-FET was carried out to analyze the reliability of Al<sub>2</sub>O<sub>3</sub> high-k dielectric. The stress was applied to gate and biased at 5.5 V. DC transfer characteristics at  $V_d = 0.5$  V were measured right after the removal of PBTI stress at room temperature. As shown in Figure 4(e), after 1000 s stress, the degradation of on-current was 3.5%, while

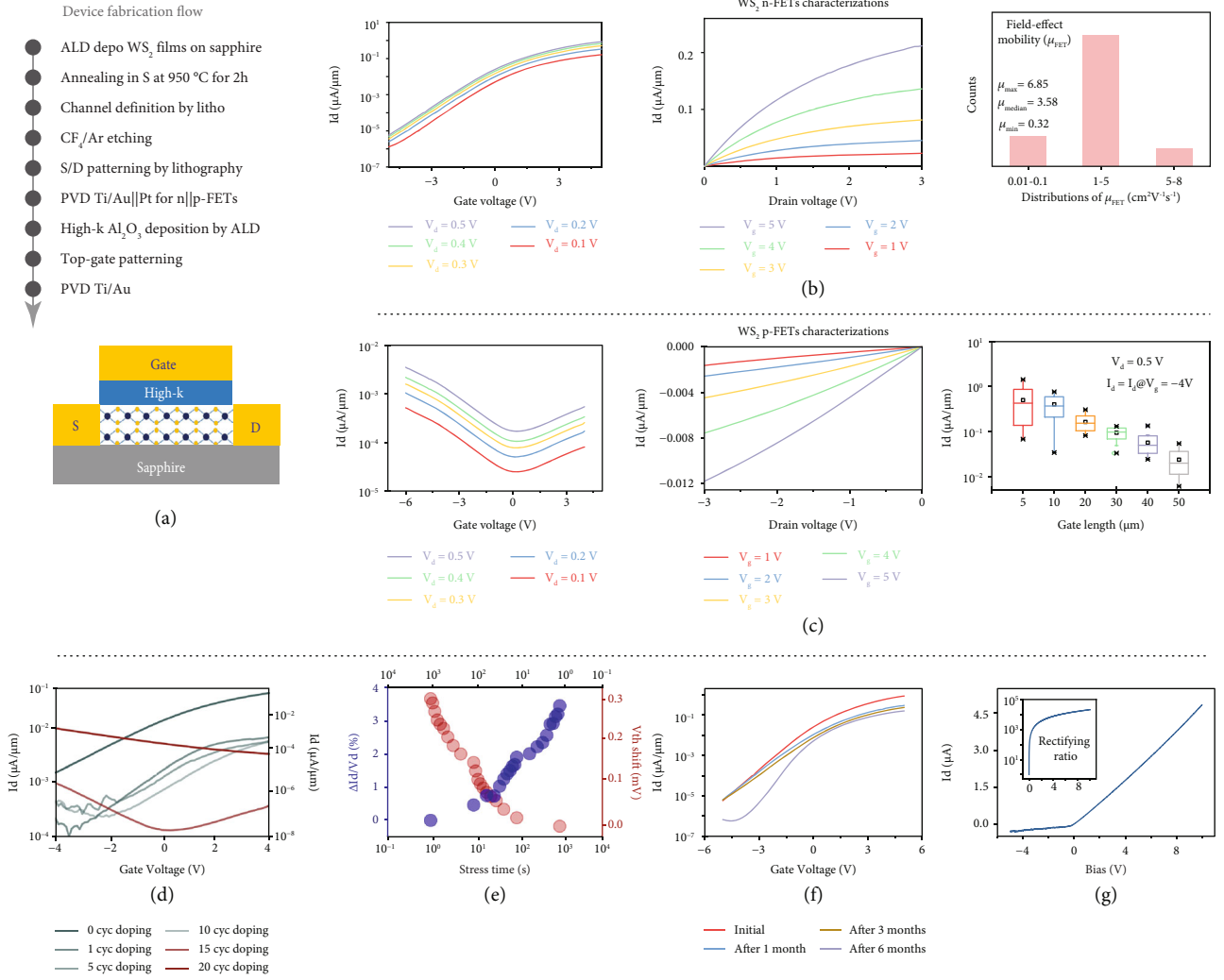


FIGURE 4: The electrical properties of  $\text{WS}_2$  n-FETs and Nb-doped  $\text{WS}_2$  p-FETs. (a) CMOS-compatible process flow of FETs and schematic of device structures. (b) The transfer and output characteristics of  $\text{WS}_2$  n-FET with  $2\text{ }\mu\text{m}$  gate width and the mobility distribution of 30  $\text{WS}_2$  n-FETs. The on-current reached  $0.4\text{ }\mu\text{A}/\mu\text{m}$ , and the on/off ratio was up to  $10^5$ . (c) The transfer and output characteristics of 15-cycle Nb-doped  $\text{WS}_2$  p-FET with  $2\text{ }\mu\text{m}$  gate width and the distribution of  $I_d$  at  $V_d = 0.5\text{ V}$  and  $V_g = -4\text{ V}$  for 132 Nb-doped  $\text{WS}_2$  p-FETs with 25-cycle Nb doping. The carrier type changed from electron to hole, and the on-current was  $5 \times 10^{-2}\text{ }\mu\text{A}/\mu\text{m}$ . (d) The doping effects on  $\text{WS}_2$  FETs. Nb dopants varied from 1 to 20 cycles. Nb-doped  $\text{WS}_2$  FET did not show p-type behavior but with a decreased on- and off-current until reaching 15 cycles. After 20-cycle Nb doping, the device presented heavily p-type behavior, indicating the controllable doping. (e) The PBTI of  $\text{WS}_2$  n-FET at RT. The stress was set to be  $5.5\text{ V}$ . After  $1000\text{ s}$  stress, the on-current degraded only for  $3.5\%$ , while the  $\Delta V_{\text{th}}$  was up to  $300\text{ mV}$ . (f) The air stability of  $\text{WS}_2$  n-FET in ambient for 1, 3, and 6 months. The on-current degraded slightly within one order, while the degradation of off-current was less obvious after 3 months than that of 6 months. (g) The I-V curve of  $\text{WS}_2/\text{Nb-doped } \text{WS}_2$  p-n structures with the rectifying ratio of over  $10^4$ . The inset figure was rectifying ratio.

the  $V_{\text{th}}$  shift was only  $300\text{ mV}$  which was  $6\%$  of max-applied gate voltage. The results implied the instability of high-k films indeed affected the electrical properties of  $\text{WS}_2$  n-FET. Higher quality high-k dielectrics would improve the electrical property of  $\text{WS}_2$  n-FET [42]. To investigate the air stability of  $\text{WS}_2$  film, the  $\text{WS}_2$  n-FET was placed in ambient atmosphere, and the transfer characteristics were tested at  $V_d = 0.5\text{ V}$  after 1 month, 3 months, and 6 months, as shown in Figure 4(f). The on-current of  $\text{WS}_2$  n-FET degraded slightly, while the degradation was within one order of magnitude even after 6-month exposure in air. However, despite the fact that the deterioration of off-

current was hardly observed after 3-month exposure, the deterioration of off-current was almost one order of magnitude after 6-month exposure. Consequently, the on/off ratio decayed from  $10^5$  to  $10^4$  after 6 months in ambient. Furthermore, vertical p-n structure based on  $\text{WS}_2$  and Nb-doped  $\text{WS}_2$  films was fabricated. The electrical property of p-n structure with rectifying ratio of  $10^4$  is shown in Figure 4(g), with an ideal factor of 2.3, indicating a conspicuous recombination of electron-hole.

The benchmark of p-type  $\text{WS}_2$  transistors is listed in Table 1, including various deposition doping methods. The CVD method could yield the highest  $I_{\text{on}}/I_{\text{off}}$  ratio by

TABLE 1: Benchmark of p-type WS<sub>2</sub> transistors.

Reference	Method of p-type doping	Growth method	Controllable doping	Wafer scale synthesis	EOT (nm)	$I_{on}/I_{off}$ at 4.6 MV/cm
Our work	Nb	ALD	√	√	13	10 <sup>1</sup>
[20]	Nb	CVD	×	×	270	<10
[36]	Nb	CVD	×	×	285	10 <sup>2</sup>
[39]	$\Phi_m$	ALD	×	√	15	10 <sup>2</sup>
[27]	$\Phi_m$	ALD	×	√	60	10 <sup>4</sup>
[28]	$\Phi_m$	CVD	×	×	5.16	10 <sup>6</sup>
[23]	CH	PECVD	×	×	32.5	10 <sup>4</sup>

$\Phi_m$  stands for adjusting metal work function (Ti et al.).

adjusting metal work function but suffers from the difficulties of large volume synthesis on 8/12-inch wafers. For ALD approach, wafer scale deposition has been studied; however, our work was the first demonstration of p-type WS<sub>2</sub> films on large-scale wafers, with *in situ* controllable doping.

### 3. Discussion

For the first time, we demonstrated the wafer-scale synthesis of WS<sub>2</sub> films by ALD with controllable *in situ* p-type doping, on 8-inch  $\alpha$ -Al<sub>2</sub>O<sub>3</sub>/Si wafer, 2-inch sapphire wafer, and pieced GaN substrates with a postannealing process. The plane-view and cross-sectional TEM indicated the successful synthesis of WS<sub>2</sub> film with the average grain size of 55 nm. The XPS spectra, Hall effect, and TOF-SIMS proved the substitutional doping of Nb. The Nb-doped WS<sub>2</sub> FETs with different Nb doping concentrations were fabricated to demonstrate the controllable Nb doping. Furthermore, the p-n structure based on WS<sub>2</sub> and Nb-doped WS<sub>2</sub> films showed 10<sup>4</sup> rectifying ratio, giving evidence to the realization of p-type WS<sub>2</sub>. Our work realized the controllable *in situ* Nb doping WS<sub>2</sub> films by ALD, which obviated the difficulty of p-type WS<sub>2</sub> film and paved a path to the fabrication of complementary WS<sub>2</sub> FETs and further applications on logic circuits.

### 4. Materials and Methods

**4.1. Material Synthesis and Characterization.** The WS<sub>2</sub> and Nb-doped WS<sub>2</sub> film were deposited on 2-inch sapphire substrate by ALD (Beneq, TFS-200). Prior to the deposition, the sapphire substrate was cleaned by acetone, ethyl alcohol, diluted HF (1:50), and deionized water in order. For Nb doping, a typical cycle includes 1 s NbCl<sub>5</sub> pulse, followed by 8 s purge (Argon, 99.99%), and 1 s HMDST pulse, followed by 5 s purge. To achieve Nb-doped WS<sub>2</sub> film, the NbS<sub>2</sub> process was sandwiched into a WS<sub>2</sub> process accordingly. Nb concentration was precisely controlled through altering NbS<sub>2</sub> cycle numbers. The cycle number of 4.6 nm WS<sub>2</sub> was 400. The as-deposited samples were put in a quartz boat placed in the center of Zone I and Zone II, and 0.5 g sulfur powder was placed in Zone III carried by a quartz boat. The samples were annealed for 2 h in a 4-inch quartz tube at the base pressure less than 0.4 Pa. The temperature of Zone I and Zone II were raised to 950°C in 55 minutes,

and the temperature of Zone III was raised to 350°C in 55 minutes. The morphology and structure of WS<sub>2</sub> and Nb-doped WS<sub>2</sub> were characterized by XPS (Augerscan-PHI5300, monochromatic Al K $\alpha$  anode at 9.97 kV and 14.7 mA as the source of X-ray radiation; pass energy was 112 eV; step was 0.1 eV, peak fitted using combined Gaussian, and Lorentzian line shapes), Raman (LabRAM, 532 nm laser wavelength, 1 mW x100\_VIS), Hall effect measurements (Lakeshore 8400, van der Pauw, DC, 4-probes), and HRTEM (Thermo Fisher Scientific Talos F200X; acceleration voltage was 200 kV; the sample was prepared by Thermo Fisher Scientific Helios G4 UX focus ion beam, and a protective layer of Pt was deposited on the surface of the sample by electron beam and ion beam).

**4.2. Device Fabrication.** Top-gate FETs for WS<sub>2</sub> and Nb-doped WS<sub>2</sub> films were fabricated through CMOS-compatible processes. After annealing in S atmosphere, photolithography was used to define channel area and was etched by CF<sub>4</sub>/Ar (20/10 sccm) in RIE. Source and drain were patterned by photolithography and metalized by Ti/Au (15/70 nm) for WS<sub>2</sub> n-FETs and Pt (70 nm) for Nb-doped WS<sub>2</sub> p-FETs by PVD (Kurt J. Lesker PVD75). A 20 nm Al<sub>2</sub>O<sub>3</sub> gate oxide was deposited by ALD at 250°C. The precursors for Al<sub>2</sub>O<sub>3</sub> were TMA and H<sub>2</sub>O, respectively. After top-gate patterning, 15/70 nm Ti/Au was deposited by PVD.

**4.3. Device Measurement.** All electrical properties of WS<sub>2</sub> n-FETs and Nb-doped WS<sub>2</sub> p-FETs were measured in ambient room temperature by the Agilent B1500A Semiconductor Device Analyzer in probe station (MPI-TS3000). The field-effect carrier mobility was extracted from the transfer characteristic using the equation  $\mu = (\Delta I_d / \Delta V_g) \times L / (WC_{ox} V_d)$ , and the  $C_{ox} = 2.656 \text{ F/m}^2$  was the unit gate capacitance between channel and top-gate ( $C_{ox} = \epsilon_1 \epsilon_0 / d$ ,  $\epsilon_1 = 6$ , and  $d = 20 \text{ nm}$  for Al<sub>2</sub>O<sub>3</sub> dielectric).

### Conflicts of Interest

The authors declare no competing financial interest.

### Authors' Contributions

Y.W., C.T., and L.J. conceived and designed the experiments. Y.W., C.T., R.B., and H.J.Y. carried out the material deposition, annealing, and device fabrication. Y.W., C.T., and



Z.C.W. carried out the I-V measurements and reliability measurements. S.H. and X.Z. contributed to material characterizations. All authors contributed to interpreting the data and writing the manuscript. Hanjie Yang, Yang Wang, Xingli Zou, and Li Ji contributed equally to this work.

## Acknowledgments

This work is partially supported by the NSFC (62004044 and 61904033) and by State Key Laboratory of ASIC & System (2021MS004). This research was partially supported by the National Science Foundation through the Center for Dynamics and Control of Materials: an NSF MRSEC under Cooperative Agreement No. DMR-1720595. Li Ji acknowledges the support of starting research fund from Fudan University and the Young Scientist Project of MOE Innovation platform. Deji Akinwande acknowledges the support of ARO via a PECASE award.

## Supplementary Materials

Fig. S1: thickness of the 400-cycle  $\text{WS}_2$  films as a function of HMDST and  $\text{WCl}_6$  precursor pulse time. Fig. S2: XPS full spectra of as-deposited and annealed  $\text{WS}_2$  films. Fig. S3: Raman spectra of as-deposited  $\text{WS}_2$  film. Fig. S4: cross-sectional TEM of 3.7 nm  $\text{WS}_2$  film. Fig. S5: grain size analysis of  $\text{WS}_2$  film. Fig. S6:  $\text{WS}_2$  film images with different cycle numbers and AFM image of 4.6 nm  $\text{WS}_2$  film. Fig. S7: XPS results of as-deposited  $\text{NbS}_2$  film. Table S1:  $\text{WS}_2$  film process cycles with different Nb doping concentrations. Fig. S8: schematic diagram of process cycle of Nb-doped  $\text{WS}_2$  film. Fig. S9: XPS full spectra of as-deposited and annealed Nb-doped  $\text{WS}_2$  films. Fig. S10: plane-view EDX mapping of Nb-doped  $\text{WS}_2$  film. Table S2: hall measurements of  $\text{WS}_2$  and Nb-doped  $\text{WS}_2$  with Nb doping of 15, 20, and 100 cycles. (*Supplementary Materials*)

## References

- [1] B. Radisavljevic and A. Kis, "Mobility engineering and a metal-insulator transition in monolayer  $\text{MoS}_2$ ," *Nature Materials*, vol. 12, no. 9, pp. 815–820, 2013.
- [2] Y. Gao, Z. Liu, D. Sun et al., "Large-area synthesis of high-quality and uniform monolayer  $\text{WS}_2$  on reusable Au foils," *Nature Communications*, vol. 6, no. 1, p. 8569, 2015.
- [3] S. Y. Kim, S. Park, and W. Choi, "Enhanced carrier mobility of multilayer  $\text{MoS}_2$  thin-film transistors by  $\text{Al}_2\text{O}_3$  encapsulation," *Applied Physics Letters*, vol. 109, no. 15, p. 152101, 2016.
- [4] L. Liu, S. B. Kumar, Y. Ouyang, and J. Guo, "Performance limits of monolayer transition metal dichalcogenide transistors," *IEEE Transactions on Electron Devices*, vol. 58, no. 9, pp. 3042–3047, 2011.
- [5] O. Lopez-Sanchez, D. Lembke, M. Kayci, A. Radenovic, and A. Kis, "Ultrasensitive photodetectors based on monolayer  $\text{MoS}_2$ ," *Nature Nanotechnology*, vol. 8, no. 7, pp. 497–501, 2013.
- [6] C. Liu, H. Chen, S. Wang, Q. Liu, and P. Zhou, "Two-dimensional materials for next-generation computing technologies," *Nature Nanotechnology*, vol. 15, no. 7, pp. 545–557, 2020.
- [7] S. Wachter, D. K. Polyushkin, O. Bethge, and T. Mueller, "A microprocessor based on a two-dimensional semiconductor," *Nature Communications*, vol. 8, no. 1, p. 14948, 2017.
- [8] R. Ge, X. Wu, L. Liang et al., "A library of atomically thin 2D materials featuring the conductive-point resistive switching phenomenon," *Advanced Materials*, vol. 33, no. 7, p. 2007792, 2020.
- [9] S. M. Hus, R. Ge, P. A. Chen et al., "Observation of single-defect memristor in an  $\text{MoS}_2$  atomic sheet," *Nature Nanotechnology*, vol. 16, no. 1, pp. 58–62, 2021.
- [10] X. Zhang, J. Grajal, J. L. Vazquez-Roy et al., "Two-dimensional  $\text{MoS}_2$ -enabled flexible rectenna for Wi-Fi-band wireless energy harvesting," *Nature*, vol. 566, no. 7744, pp. 368–372, 2019.
- [11] Q. Gao, Z. Zhang, X. Xu, J. Song, X. Li, and Y. Wu, "Scalable high performance radio frequency electronics based on large domain bilayer  $\text{MoS}_2$ ," *Nature Communications*, vol. 9, no. 1, p. 4778, 2018.
- [12] K. Myungsoo, R. Ge, X. Wu et al., "Zero-static power radio-frequency switches based on  $\text{MoS}_2$  atomrystors," *Nature Communications*, vol. 9, no. 1, p. 2524, 2018.
- [13] H. Zhang, "Ultrathin two-dimensional nanomaterials," *ACS Nano*, vol. 9, no. 10, pp. 9451–9469, 2015.
- [14] S. Wang, C. Chen, Z. Yu et al., "A  $\text{MoS}_2$ /PTCDA hybrid heterojunction synapse with efficient photoelectric dual modulation and versatility," *Advanced Materials*, vol. 31, no. 3, p. 1806227, 2019.
- [15] C. Cong, J. Shang, W. Xing et al., "Synthesis and optical properties of large-area single-crystalline 2D semiconductor  $\text{WS}_2$  monolayer from chemical vapor deposition," *Advanced Optical Materials*, vol. 2, no. 2, pp. 131–136, 2014.
- [16] M. Okada, T. Sawazaki, K. Watanabe et al., "Direct chemical vapor deposition growth of  $\text{WS}_2$  atomic layers on hexagonal boron nitride," *ACS Nano*, vol. 8, no. 8, pp. 8273–8277, 2014.
- [17] C. Lan, Z. Zhou, Z. Zhou et al., "Wafer-scale synthesis of monolayer  $\text{WS}_2$  for high-performance flexible photodetectors by enhanced chemical vapor deposition," *Nano Research*, vol. 11, no. 6, pp. 3371–3384, 2018.
- [18] U. P. Rathod, J. Egede, A. A. Voevodin, and N. D. Shepherd, "Extrinsic p-type doping of few layered  $\text{WS}_2$  films with niobium by pulsed laser deposition," *Applied Physics Letters*, vol. 113, no. 6, article 062106, 2018.
- [19] D. Chu and E. K. Kim, "Hole conduction of tungsten diselenide crystalline transistors by niobium dopant," *Advanced Electronic Materials*, vol. 5, no. 2, p. 1800695, 2019.
- [20] Y. Jin, Z. Zeng, Y. Lin et al., "Synthesis and transport properties of degenerate P-type Nb-doped  $\text{WS}_2$  monolayers," *Chemistry of Materials*, vol. 31, no. 9, pp. 3534–3541, 2019.
- [21] M. Li, J. Yao, X. Wu, S. Zhang, and Y. Wang, "P-type doping in large-area monolayer  $\text{MoS}_2$  by chemical vapor deposition," *ACS Applied Materials & Interfaces*, vol. 12, no. 5, pp. 6276–6282, 2020.
- [22] H. Fang, S. Chuang, T. Chang, K. Takei, T. Takahashi, and A. Javey, "High-performance single layered  $\text{WSe}_2$  p-FETs with chemically doped contacts," *Nano Letters*, vol. 12, no. 7, pp. 3788–3792, 2012.
- [23] F. Zhang, Y. Lu, D. S. Schulman et al., "Carbon doping of  $\text{WS}_2$  monolayers: bandgap reduction and p-type doping transport," *Science Advances*, vol. 5, no. 5, p. eaav5003, 2019.



- [24] M. S. Choi, D. Qu, D. Lee, X. Liu, and W. Yoo, "Lateral MoS<sub>2</sub> p-n junction formed by chemical doping for use in high-performance optoelectronics," *ACS Nano*, vol. 8, no. 9, pp. 9332–9340, 2014.
- [25] S. Mouri, Y. Miyauchi, and K. Matsuda, "Tunable photoluminescence of monolayer MoS<sub>2</sub> via chemical doping," *Nano Letters*, vol. 13, no. 12, pp. 5944–5948, 2013.
- [26] S. Chuang, C. Battaglia, A. Azcatl et al., "MoS<sub>2</sub> P-type transistors and diodes enabled by high work function MoOx contacts," *Nano Letters*, vol. 14, no. 3, pp. 1337–1342, 2014.
- [27] C. Huyghebaert, T. Schram, Q. Smets et al., "2D materials: roadmap to CMOS integration," in *2018 IEEE International Electron Devices Meeting (IEDM)*, San Francisco, CA, USA, December 2018.
- [28] C.-C. Cheng, Y.-Y. Chung, U.-Y. Li et al., "First demonstration of 40-nm channel length top-gate WS<sub>2</sub> pFET using channel area-selective CVD growth directly on SiO<sub>2</sub>/Si substrate," in *2019 Symposium on VLSI Technology*, Kyoto, Japan, June 2019.
- [29] J. Song, J. Park, W. Lee et al., "Layer-controlled, wafer-scale, and conformal synthesis of tungsten disulfide nanosheets using atomic layer deposition," *ACS Nano*, vol. 7, no. 12, pp. 11333–11340, 2013.
- [30] M. Delabie, M. Caymax, B. Groven et al., "Low temperature deposition of 2D WS<sub>2</sub> layers from WF<sub>6</sub> and H<sub>2</sub>S precursors: impact of reducing agents," *Chemical Communications*, vol. 51, no. 86, pp. 15692–15695, 2015.
- [31] A. N. Groven, H. Mehta, J. Bender et al., "Two-dimensional crystal grain size tuning in WS<sub>2</sub> atomic layer deposition: an insight in the nucleation mechanism," *Chemistry of Materials*, vol. 30, no. 21, pp. 7648–7663, 2018.
- [32] A. N. Groven, H. Mehta, Q. Bender et al., "Nucleation mechanism during WS<sub>2</sub> plasma enhanced atomic layer deposition on amorphous Al<sub>2</sub>O<sub>3</sub> and sapphire substrates," *Journal of Vacuum Science and Technology A*, vol. 36, no. 1, p. 01A105, 2018.
- [33] J. Suh, T. Park, D. Lin et al., "Doping against the native propensity of MoS<sub>2</sub>: degenerate hole doping by cation substitution," *Nano Letters*, vol. 14, no. 12, pp. 6976–6982, 2014.
- [34] Y. Zhang, L. Yin, J. Chu et al., "Edge-epitaxial growth of 2D NbS<sub>2</sub>-WS<sub>2</sub> lateral metal-semiconductor heterostructures," *Advanced Materials*, vol. 30, no. 40, p. 1803665, 2018.
- [35] H. R. Gutierrez, N. Perea-Lopez, A. L. Elias et al., "Extraordinary room-temperature photoluminescence in triangular WS<sub>2</sub> monolayers," *Nano Letters*, vol. 13, no. 8, pp. 3447–3454, 2013.
- [36] X. Li, M. Lin, L. Basile et al., "Isoelectronic tungsten doping in monolayer MoSe<sub>2</sub> for carrier type modulation," *Advanced Materials*, vol. 28, no. 37, pp. 8240–8247, 2016.
- [37] B. Groven, M. Heyne, K. Haesevoets et al., "Plasma-enhanced atomic layer deposition of two-dimensional WS<sub>2</sub> from WF<sub>6</sub>, H<sub>2</sub> plasma, and H<sub>2</sub>S," *Chemistry of Materials*, vol. 29, no. 7, pp. 2927–2938, 2017.
- [38] T. Schram, Q. Smets, B. Groven et al., "WS<sub>2</sub> transistors on 300 mm wafers with BEOL compatibility," in *2017 47th European Solid-State Device Research Conference (ESSDERC)*, Leuven, Belgium, September 2017.
- [39] V. Vandalon, M. Verheijen, W. Kessels, and A. Bol, "Atomic layer deposition of Al-doped MoS<sub>2</sub>: synthesizing a p-type 2D semiconductor with tunable carrier density," *ACS Applied Nano Materials*, vol. 3, no. 10, pp. 10200–10208, 2020.
- [40] R. V. Kasowski, "Band structure of MoS<sub>2</sub> and NbS<sub>2</sub>," *Physical Review Letters*, vol. 30, no. 23, pp. 1175–1178, 1973.
- [41] G. Nazir, M. F. Khan, V. M. Iermolenko, and J. Eom, "Two- and four-probe field-effect and Hall mobilities in transition metal dichalcogenide field-effect transistors," *RSC Advances*, vol. 6, no. 65, pp. 60787–60793, 2016.
- [42] T. Park, H. Kim, M. Leem et al., "Atomic layer deposition of Al<sub>2</sub>O<sub>3</sub> on MoS<sub>2</sub>, WS<sub>2</sub>, WSe<sub>2</sub>, and h-BN: surface coverage and adsorption energy," *RSC Advances*, vol. 7, no. 2, pp. 884–889, 2017.